Article

Pyro-Phototronic Effect Enhanced MXene/ZnO Heterojunction Nanogenerator for Light Energy Harvesting

Mingyan Xue [1,2], Fangpei Li [1,2,3,*], Wenbo Peng [1,2,*], Quanzhe Zhu [4] and Yongning He [1,2,*]

1   School of Microelectronics, Xi'an Jiaotong University, Xi'an 710049, China
2   The Key Lab of Micro-Nano Electronics and System Integration of Xi'an City, Xi'an 710049, China
3   State Key Laboratory of Solidification Processing, Key Laboratory of Radiation Detection Materials and Devices, School of Materials Science and Engineering, Northwestern Polytechnical University, Xi'an 710072, China
4   Shaanxi Advanced Semiconductor Technology Center Co., Ltd, Xi'an 710077, China
*   Correspondence: fangpeilee@163.com (F.L.); wpeng33@mail.xjtu.edu.cn (W.P.); yongning@mail.xjtu.edu.cn (Y.H.)

Abstract: The coupling of pyroelectricity, semiconductor, and optical excitation yields the pyro-phototronic effect, which has been extensively utilized in photodetectors. It can also enhance the performance of light energy harvesting nanogenerators. In this work, a pyro-phototronic effect-enhanced MXene/ZnO heterojunction nanogenerator has been successfully demonstrated, which can harvest broadband light energy (from deep UV to near-infrared) and still operate at 200 °C. The morphology of the ZnO layer and the MXene layer's thickness have been further optimized for better light energy harvesting performance. For the optimized heterojunction nanogenerator, the responsivity can be improved from ~0.2 mA/W to ~3.5 mA/W by pyro-phototronic effect, under 0.0974 mW/cm^2 365 nm UV illumination. Moreover, the coupling of pyro-phototronic and piezo-phototronic effects in MXene/ZnO heterojunction nanogenerators has been investigated. The results indicate that only a small tensile strain could improve the nanogenerator's performance. The working mechanisms have been carefully analyzed, and the modulation of piezoelectric charges on the Schottky barrier height is found to be the key factor. These results demonstrate the enormous potential of the pyro-phototronic effect in light energy harvesting nanogenerators and illustrate the coupling of pyro-phototronic and piezo-phototronic effects for further performance improvement.

Keywords: pyro-phototronic; MXene; ZnO; nanogenerator; piezo-phototronic

1. Introduction

A nanogenerator is a device capable of harvesting ambient energies and converting them into electricity [1–4]. Being invented in 2006 for the first time by Prof. Zhong Lin Wang, it is composed of ZnO nanowires (NWs) and designed for harvesting mechanical energy [5]. With an atomic force microscopy (AFM) tip scanning across the ZnO NWs, mechanical energy is converted into electricity by the piezoelectric effect of ZnO. The fields of nanogenerators develop very quickly and in 2012, Prof. Zhong Lin Wang discovered the triboelectric nanogenerator (TENG) [6]. TENG utilizes triboelectrification to produce electricity and originates from Maxwell's displacement current [7–10]. Consequently, TENG could scavenge nearly all kinds of mechanical energies, including vibration [11–15], sound [16–18], walking [19], running [20], wind [21], and even blue energy [22–25]. Oceans have colossal energy, and they offer the possibility of substituting fossil energy in the future. However, harvesting water wave energy from the sea is challenging because of the low frequency, wide distribution, and complex environment. TENG has outstanding energy harvesting performances at low frequency and low impact conditions, making it a superior candidate for harvesting ocean water wave energy, which is also referred to as blue energy. In addition to mechanical energy, thermal energy could also be harvested by

nanogenerators based on the pyroelectric effect [26]. Several pyroelectric nanogenerators have been designed and reported to effectively harvest thermal energy induced by ambient temperature variations [27–30].

Coupled with semiconductor and optical excitation, pyroelectricity has been proven to significantly improve the photodetector's performance [31]. In 2015, a perovskite/ZnO heterojunction with photocurrent improvement by pyroelectricity was reported for the first time [31]. The three-field coupling effect has been named the pyro-phototronic effect, i.e., utilizing the light itself induced heating ability to produce a pyroelectric effect and then modulate the photodetector's performances [31,32]. A lot of research has been conducted on the pyro-phototronic effect in the past few years, from the temperature dependence [33,34] and different materials [35,36] to device structure optimization [37,38] and broadband light response [39,40]. It is shown that a lower ambient temperature is preferred for a better pyro-phototronic effect [33]. This is well-accepted as the light heating would be more obvious at lower ambient temperatures. It is also proved that the thickness of the material chosen for the pyro-phototronic effect should be neither too large nor too small [37]. Though the pyro-phototronic effect has been extensively utilized in the photodetector, there are just a few researches focusing on its application in light energy harvesting nanogenerators.

Since ZnO is a promising wide bandgap semiconductor material that simultaneously owns piezoelectricity and pyroelectricity [41–43], it has become famous in the research fields of piezo-phototronics and pyro-phototronics [44,45]. In addition, compared to other semiconductor materials that also own piezoelectricity and pyroelectricity, for instance, GaN and CdS, the syntheses of ZnO and its nanostructures are much more feasible. The growth of GaN or CdS typically requires either high temperature or high pressure, whereas ZnO and its nanostructures can be grown at low temperature (<100 °C) and ambient pressure [46–48]. Meanwhile, as a new member of two-dimensional materials, MXene exhibits high electrical conductivity, electronegativity, good mechanical stability, etc., and consequently has been vastly demonstrated in nanogenerators for energy conversion improvement [49–51]. Moreover, MXene also has fascinating thermal conductivity, which is promising in fabricating high-performance pyro-phototronic nanogenerators as the pyro-phototronic effect is dominated by the light-induced transient temperature variation [52–56]. Considering all the advantages discussed above, an MXene/ZnO heterojunction device should be a promising candidate as a pyro-phototronic nanogenerator.

In this work, by sputtering a ZnO thin film and spin-coating an MXene layer consequently on an ITO/glass substrate, an MXene/ZnO heterojunction nanogenerator for light energy harvesting is fabricated. Its response to 254, 365, and 405 nm illuminations has been characterized. Then, the performances of the nanogenerator and the pyro-phototronic effect-induced improvement were systematically investigated for different light wavelengths. The results indicate that the pyro-phototronic effect could improve the performances of nanogenerators significantly. The working temperature of nanogenerators has also been studied, and the results show that it could still work at 200 °C high temperature. Furthermore, the influences of ZnO's morphology and MXene's thickness have been studied and optimized. Finally, by fabricating a flexible MXene/ZnO heterojunction nanogenerator on an ITO/PET substrate, the coupling between pyro-phototronic and piezo-phototronic effects has been studied experimentally and analyzed theoretically. This work not only demonstrates the huge potential of the pyro-phototronic effect in light energy harvesting nanogenerators but also illustrates the coupling of pyro-phototronic and piezo-phototronic effects for further performance improvement.

2. Materials and Methods

In the experiment, ITO (Indium Tin Oxide) conductive glass (square resistance < 10 ohm/sq, transmittance ≥ 83%) was selected, and it was cleaned with ultra-sonication for 5 min each with acetone, ethanol, and deionized water. The tape was used to cover part of the ITO region as the bottom electrode. Then, different morphologies of ZnO layers were obtained by different methods.

A 100 nm ZnO seed layer was first deposited on an ITO/glass substrate by radio frequency (RF) magnetron sputtering (Model GJP-450) at room temperature, and the ZnO-seed-coated ITO/glass was then placed in a different mixed nutrient solution for further growth of ZnO nanowires. ZnO nanowires (NWs) were grown by a hydrothermal heating method in a mechanical convection oven (Model STH120). Four mixed nutrient solutions have been prepared to evaluate the influence of ZnO NWs' morphology on the performance of the MXene/ZnO heterojunction pyro-phototronic nanogenerator.

For the first group (marked as #1), 25 mM $Zn(NO_3)_2$ and 12.5 mM HMTA were prepared and well mixed as the nutrient solution, and 5.4 mL of ammonium hydroxide (Alfa Aesar) was added per 100 mL of mixed nutrient solution. The ZnO seed layer coated ITO/glass substrate was then placed to float on the surface of the mixed nutrient solution with the ZnO seed layer facing down and in contact with the mixed nutrient solution. Then, the whole mixed nutrient solution together with floating ZnO seed-coated ITO/glass substrate was heated to 95 °C and kept at 95 °C for 1 h (i.e., the growth time of ZnO NWs). After the entire system was cooled down to room temperature, the samples were cleaned with deionized water and dried with high-purity nitrogen.

For the second group (marked as #2), 25 mM $Zn(NO_3)_2$ and 25 mM HMTA were prepared and well mixed as the nutrient solution without ammonium hydroxide. The growth processes of ZnO NWs are exactly the same as described in Group #1. The only difference is that the temperature is set to 80 °C and the growth time is 3 h.

Then, the concentration of the mixed nutrient solution was changed to 50 mM and 100 mM in another two groups (marked as #3 and #4, separately). The growth temperature and time are set as 80 °C and 3 h, and all the other parameters are also kept the same as in Group #2.

Finally, a group (marked as #5) only using ZnO thin film was prepared for comparison. The ZnO thin film was directly deposited on the ITO/glass substrate by RF magnetron sputtering (GDP-450). During the sputtering, the chamber pressure was kept at 1.0 Pa, the power was 120 W, the temperature was room temperature, and the growth time period was 30 min. The oxygen and argon gases with a ratio of O_2:Ar = 1:2 were injected into the chamber as reacting and carrying gases, respectively.

The MXene utilized in our experiments is purchased from Nanjing XFNANO Materials Tech Co., Ltd. (Nanjing, China). The $Ti_3C_2T_x$ MXene thin layer (number of layers is approximately 1~5) dispersion solution, with a concentration of 2.5 mg/mL and solvent of water, is purchased and directly utilized in the experiments without any further treatment. The fabrication process of the MXene layer on ZnO is described as follows: First, the ZnO NWs (or ZnO thin film) coated ITO/glass substrate was fixed on a planar plate for the spin-coating of the MXene layer. Next, 5 μL of the purchased $Ti_3C_2T_x$ MXene thin layer dispersion liquid was taken by pipette. Then, the liquid was dropped onto ZnO and the planar plate was controlled to rotate at a rotation speed of 1000 rpm for 1 min. After the rotation, the substrate was kept at room temperature in the normal ambient environment for 15 min. The moisture in the liquid was dried naturally, and finally, the $Ti_3C_2T_x$ MXene layer was formed on ZnO.

To investigate the influence of the spin-coated MXene layer's thickness on the performance of the MXene/ZnO heterojunction pyro-phototronic nanogenerator, the rotation speed was altered to 800 rpm, 500 rpm, and 0 rpm, respectively. It is worth noting that a rotation speed of 0 rpm indicates no rotation at all, and the substrate was directly kept at room temperature for 15 min after the liquid dropped onto ZnO. Therefore, an increase in the thickness of the MXene layer with a decrease in the rotation speed can be expected. The test wires were connected to the $Ti_3C_2T_X$ MXene film and the bottom ITO by silver paste.

For flexible devices, ITO/PET (polyethylene terephthalate film) flexible conductive film (square resistance: 60 ohm/sq) was purchased from Sigma Aldrich (Shanghai, China) and directly used as the substrate without any further treatment. It was first cleaned with ultrasonication for 5 min each with acetone, ethanol, and deionized water. Then, ZnO thin film was obtained by RF magnetron sputtering (GDP-450) on ITO/PET for 30 min

at room temperature with the same parameters, and flexible MXene/ZnO heterojunction was obtained by using a 1000 rpm homogenizer. The test wires were connected to the $Ti_3C_2T_X$ MXene film and the bottom ITO region by silver paste. The effective area of the ITO/glass substrate-based devices is fixed at 5 mm × 10 mm. The effective area of the flexible ITO/PET substrate-based devices is fixed at 3.75 mm × 10 mm. For all the devices based on both substrates, the whole area of devices is illuminated by the incident light, meaning that the effective area of devices and the area of illumination are the same.

The microstructures of the $Ti_3C_2T_X$ MXene layer, ZnO NWs, and ZnO thin film were characterized by scanning electron microscopy (SEM) (GeminiSEM 500, ZEISS, Oberkochen, Germany). The crystal structure, element analysis, and photoluminescence (PL) of spin-coated $Ti_3C_2T_X$ MXene and ZnO layers were characterized. The X-ray diffraction (XRD) characterization was conducted by a Bruker D8 ADVANC diffractometer. The X-ray photoelectron spectroscopy (XPS) characterization was carried out by Thermo Fisher ESCALAB Xi+, Waltham, MA, USA. The PL characterization was realized by HORIBA LabRAM Odyssey Nano, Kyoto, Japan, utilizing a He-Cd 325 nm laser as the excitation source.

The electrical signals of the devices were measured and recorded by a two-channel precision source/measure unit set (B2902A, Keysight, Santa Rosa, CA, USA). Optical input was provided by commonly seen light sources and lasers (wavelengths of 254 nm, 365 nm, 405 nm, and others). The UV light sources (254 nm and 365 nm) were provided by a handheld UV lamp (Model WFH-204B, Shanghai Xu Chang, Shanghai, China). The power density was controlled by modulating the distance between the lamp and the device. The 405 nm light source was provided by a semiconductor laser (Model M-16A405-100-GLX, MTO-laser, Guangzhou, China). Four other semiconductor lasers (532, 648, 780, and 830 nm) were also purchased from MTO-laser. A continuously variable filter (OMMB-NDFC50, Zolix, Xi'an, China) was used to control the power density.

3. Results and Discussion

The device structure of MXene/ZnO heterojunction fabricated on an ITO/glass substrate is schematically shown in Figure 1a, composed of the stacking of a spin-coated MXene layer on a ZnO layer. As described above in the Section 2, first, the MXene/ZnO heterojunction based solely on sputtered ZnO thin film is fabricated and studied. The rotation speed during the spin-coating of MXene is controlled at 1000 rpm, and the sputtering time of ZnO thin film is 30 min. Figure 1b,c present the top and cross-sectional SEM images of as-fabricated MXene/ZnO heterojunction. It is clearly shown that the surface morphology of the spin-coated MXene layer is smooth and uniformly distributed. Moreover, it forms a good contact with the bottom sputtered ZnO thin-film layer. The thickness of the ZnO thin film is ~165.9 nm and that of the top MXene layer is ~35 nm, due to the rotation speed during the spin-coating being relatively high.

The XRD and XPS characterizations of MXene/ZnO heterojunction have been conducted, and the results are shown in Figure S1. As clearly presented in Figure S1a, the XRD result shows a distinctive peak at $2\theta \approx 6.7°$, corresponding to the (002) peak of the $Ti_3C_2T_x$ MXene [57,58]. The XRD result also shows a sharp peak at $2\theta \approx 34.5°$, corresponding to the (002) peak of the ZnO. Other peaks are recognized from the soda-lime glass substrate, which is used to prepare MXene/ZnO heterojunction for the characterization. The XRD result verifies the existence of a spin-coated MXene layer and indicates the good crystalline structure of wurtzite ZnO, which owns *c*-axis orientation and excellent piezoelectricity and pyroelectricity.

Figure S1b shows the high-resolution XPS spectra of ZnO O1s, which have three fitted Gaussian peaks, corresponding to the lattice oxygen ($O_{Lattice}$), oxygen vacancy (V_O), and chemically absorbed oxygen (OH^-), respectively [59,60]. The area of $O_{Lattice}$ is the largest while V_O's is the smallest, implying an excellent crystalline structure. Figure S1c,d show the high-resolution XPS spectra of $Ti_3C_2T_x$ C1s and O1s. The C and Ti elements should be originated from the $Ti_3C_2T_x$ MXene itself. The O element could originate from the oxidation of $Ti_3C_2T_x$ MXene or beneath the ZnO. The C1s fitting indicates that the C–C

bond is the most, and others are the C–Ti and C–O bonds [58]. The O1s fitting illustrates that the bonding to Ti_3C_2 and Ti is the dominant, while only a very small portion comes from absorbed H_2O [58]. These XPS results show the good formation of the MXene/ZnO heterojunction, which is important for pyro-phototronic nanogenerators.
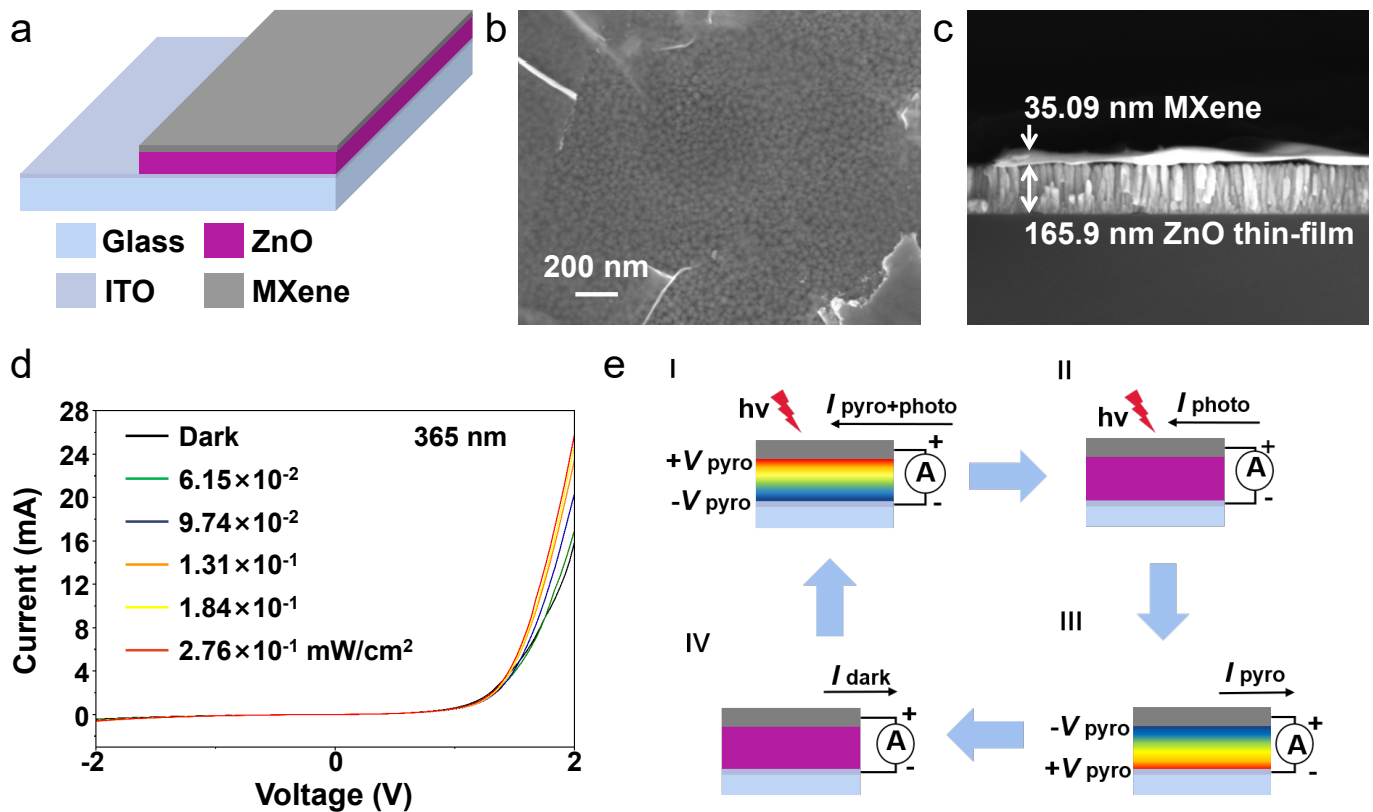

Figure 1. Fundamentals of MXene/ZnO heterojunction nanogenerator: (**a**) the device structure, (**b**) top view of SEM image, (**c**) cross–sectional view of SEM image, (**d**) I–V characteristics under 365 nm UV illumination with different power densities, and (**e**) working mechanism of pyro-phototronic effect.

The PL property of MXene/ZnO heterojunction has been characterized and the result is shown in Figure S2. The PL spectrum of MXene/ZnO heterojunction in Figure S2 obviously presents a strong peak around 400 nm, which should correspond to ZnO. There are also a few very small and wide peaks that exist in the visible and near-infrared regions, which indicates the possible existence of sub-band energy levels originating from the oxygen vacancies in ZnO and other defects. These PL spectrum results clearly illustrate the excellent response of MXene/ZnO heterojunction to UV illumination and also the possibility of responding to visible and near-infrared illuminations.

Then, the current–voltage (I–V) characteristics of MXene/ZnO heterojunction are measured under dark conditions and 365 nm UV illumination, as shown in Figure 1d. From the measured I–V results, the MXene/ZnO heterojunction shows good rectification behavior, indicating good electrical contact between MXene and ZnO. Under 365 nm UV illumination, the MXene/ZnO heterojunction presents obvious photoresponse at forward bias, where the current at +2 V bias increases dramatically from ~15 mA under dark conditions to ~25 mA under 0.276 mW/cm² 365 nm UV illumination.

From the I–V curves in Figure 1d, the rectification ratio of MXene/ZnO heterojunction under different power densities is derived, summarized, and plotted. The results are shown in Figure S3. It is obvious that the rectification ratio of MXene/ZnO heterojunction is around 40 and increases only a little as the power density of illumination increases. These results indicate that the spin-coated MXene layer has a good Schottky contact with the

synthesized ZnO layer and the fabricated MXene/ZnO heterojunction responds well to the illuminated UV light.

To demonstrate the transient photoresponse of MXene/ZnO heterojunction, its time-dependent currents at 0 V bias (i.e., at self-powered mode, which could also be recognized as a nanogenerator harvesting light energy) under 365 nm UV illumination with different power densities have been characterized and plotted in Figure 2a. From the measured results, the transient current shows a clear four-stage behavior, which directly corresponds to the pyro-phototronic effect. The fundamental mechanism is illustrated in Figure 1e. Once the incident light is absorbed by the MXene/ZnO heterojunction, the photon energy produces photogenerated electrons and holes in ZnO. Simultaneously, the temperature of ZnO would also increase to some degree, yielding a positive transient temperature rise rate $dT/dt > 0$. Considering that ZnO is a pyroelectric semiconductor, this positive dT/dt would produce a transient pyroelectric current spike, which is clearly stage I. As the light keeps illuminating, the temperature of ZnO surely saturates to a stable value, indicating that $dT/dt = 0$. As a result, the pyroelectric current spike disappears, and the current of MXene/ZnO then decreases to saturation, which should be induced by the photovoltaic effect (stage II). To better recognize these different current components, the pyroelectric current spike is named as I_{pyro}, and the photovoltaic effect-induced current is named as I_{photo}. Therefore, the total current at stage I should be the sum of them, which is named as $I_{pyro+photo} = I_{pyro} + I_{photo}$, indicating the cooperation of pyroelectric and photovoltaic effects, i.e., the pyro-phototronic effect. Stage III is actually the reverse part of the stage I. When the illumination is off, the temperature of ZnO decreases, and it yields a negative transient temperature fall rate $dT/dt < 0$. Consequently, a reverse transient pyroelectric current spike occurs at stage III. Surely, the temperature of ZnO would quickly become stable, and thus, dT/dt goes back to zero again under dark conditions, meaning that the total current recovers to the dark current (stage IV). These results demonstrate that the pyro-phototronic effect could significantly enhance the photoresponse of MXene/ZnO heterojunction and hence the performance of light energy harvesting nanogenerators.

As clearly shown in Figure 2a, both the $I_{pyro+photo}$ and I_{photo} increase with the power density of 365 nm incident light. This is reasonable since the temperature variation of ZnO as well as the photovoltaic effect should be much stronger under a larger power density of illumination. The three current components have been derived and plotted together as a function of the power density of 365 nm incident light in Figure 2b. With the increment of power density, I_{photo} only increases slightly, whereas $I_{pyro+photo}$ as well as I_{pyro} has a significant enhancement, rising from ~-40 nA to ~-140 nA, while the power density ranging from 0.0615 mW/cm^2 to 0.276 mW/cm^2. Evidently, the photovoltaic effect-induced current I_{photo} is much smaller than the pyroelectric current I_{pyro}, and as a consequence, the total current $I_{pyro+photo}$ is mainly contributed by the pyroelectric effect. These results quantitatively prove the prominent enhancement of light energy harvesting nanogenerators.

The sensitivity of a photodetector could be expressed by different figures of merits, including responsivity, detectivity, and on/off ratio. Here, the on/off ratio is calculated as the sensitivity by $I_{pyro+photo}/I_{dark}$, I_{pyro}/I_{dark}, and I_{photo}/I_{dark}, respectively. The sensitivity of fabricated MXene/ZnO heterojunction is then derived, calculated, and plotted in Figure S4. From Figure S4, obviously, the sensitivity increases with the power density and is significantly improved by the pyro-phototronic effect. The sensitivity is enhanced from 1.3 to 17.3 under 0.2761 mW/cm^2 illumination, indicating the great potential of the pyro-phototronic effect in nanogenerators.
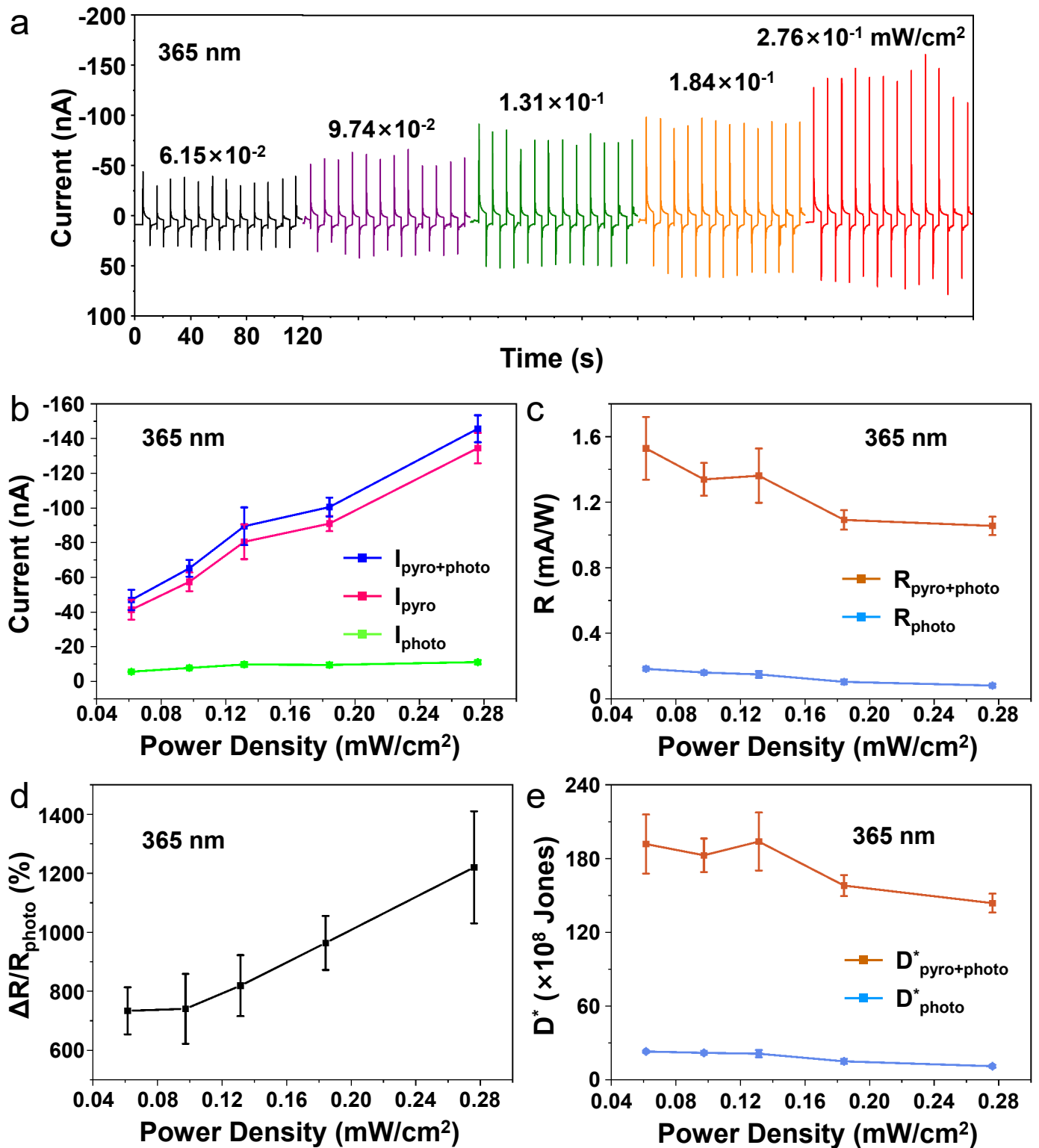
Figure 2. Pyro-phototronic effect in MXene/ZnO heterojunction nanogenerator: (**a**) transient current at 0 V bias under 365 nm illumination with different power densities, (**b**) three current components under 365 nm illumination, (**c**) responsivity and (**d**) its relative variation under 365 nm illumination, and (**e**) the specific detectivities under 365 nm illumination.

In addition to the current and sensitivity, the other two parameters are also valuable to evaluate the performance of MXene/ZnO heterojunction light energy harvesting nanogenerators: the responsivity R and the specific detectivity D*, which are also the key figures of

merit of a photodetector. Here, R is defined as $R_{pyro+photo} = I_{pyro+photo}/(P_{light} \times S)$ for pyro-phototronic effect and $R_{photo} = I_{photo}/(P_{light} \times S)$ for only photovoltaic effect, where P_{light} is the power density of incident light, and S is the effective area of MXene/ZnO heterojunction. In this work, the specific detectivity D* is calculated by considering the dark current as the main contributor to noise. So, D* is defined as $D*_{pyro+photo} = R_{pyro+photo}/(2q \times I_{dark}/S)^{0.5}$ for pyro-phototronic effect and $D*_{photo} = R_{photo}/(2q \times I_{dark}/S)^{0.5}$ for only photovoltaic effect, where q is the element charge and I_{dark} is the dark current of MXene/ZnO heterojunction as the main noise source. The responsivity, its relative variation $\Delta R/R_{photo} = (R_{pyro+photo} - R_{photo})/R_{photo}$, and detectivity as a function of power density of 365 nm incident light are calculated and plotted in Figure 2c–e, respectively. Compared to photovoltaic effect-induced R_{photo} and $D*_{photo}$, the pyro-phototronic effect has brought dramatic improvements. R has been improved from ~0.1 mA/W to ~1.3 mA/W (by averaging over all the power densities) and D from ~20×10^8 Jones to ~160×10^8 Jones (by averaging over all the power densities). Moreover, it is worth noting that, as illustrated in Figure 2d, $\Delta R/R_{photo}$ increases monotonously with a power density of 365 nm UV illumination. This phenomenon should be attributed to the excellent absorption of UV light of ZnO, due to its wide bandgap of ~3.4 eV. Once the power density of 365 nm UV illumination increases, more electrons and holes are generated, and a larger temperature variation rate dT/dt is induced, leading to the increase in relative variation of responsivity. The maximum enhancement in responsivity by the pyro-phototronic effect reaches over 1200%. These improvements in R and D* further validate the outstanding role the pyro-phototronic effect plays in light energy harvesting nanogenerators.

Furthermore, the MXene/ZnO heterojunction nanogenerator's response to 254 nm deep UV and 405 nm visible illuminations are measured. As shown in Figure S5a,d, the as-fabricated MXene/ZnO heterojunction also presents good photoresponses to 254 and 405 nm illuminations at forward bias. Figure 3a,d show the transient current at 0 V bias in response to the two illuminations with different power densities. Similar to the results in Figure 2a, the current also shows distinctive four-stage behavior and increases with power density. As summarized in Figure 3b,e, $I_{pyro+photo}$ increases from ~−20 nA to ~−60 nA for 254 nm illumination and from ~−10 nA to ~−200 nA for 405 nm illumination, respectively. The responsivities under 254 and 405 nm illuminations and their relative variations are further calculated and summarized in Figure S5b,c,e,f. These results once again prove the evident enhancement by the pyro-phototronic effect. Compared to R_{photo}, $R_{pyro+photo}$ still exhibits a large increase. However, it is notable that the relative variation of responsivity decreases with power density for 254 nm illumination and randomly changes with power density for 405 nm illumination. These different phenomena should have resulted from the weak heating ability of 254 nm illumination and the weak absorption of 405 nm illumination in ZnO. In the case of 254 nm deep UV illumination, $I_{pyro+photo}$ first increases and then quickly rises to saturation while increasing power density. But I_{photo} increases steadily with power density, finally resulting in a decrease in the relative variation of responsivity as shown in Figure S5c. In the case of 405 nm visible illumination, though the $I_{pyro+photo}$ increases monotonously to over ~−200 nA, it is achieved under a large power density of 13.2 mW/cm^2. Thus, the $R_{pyro+photo}$ falls quickly with power density. Meanwhile, considering the fact that R_{photo} also decreases with power density, the relative variation of responsivity randomly changes as shown in Figure S5f. The specific detectivity D* of the MXene/ZnO heterojunction nanogenerator under 254 and 405 nm illuminations exhibits similar dependence on the power density and also great enhancement by the pyro-phototronic effect compared to the photovoltaic effect, as clearly presented in Figure 3c,f.
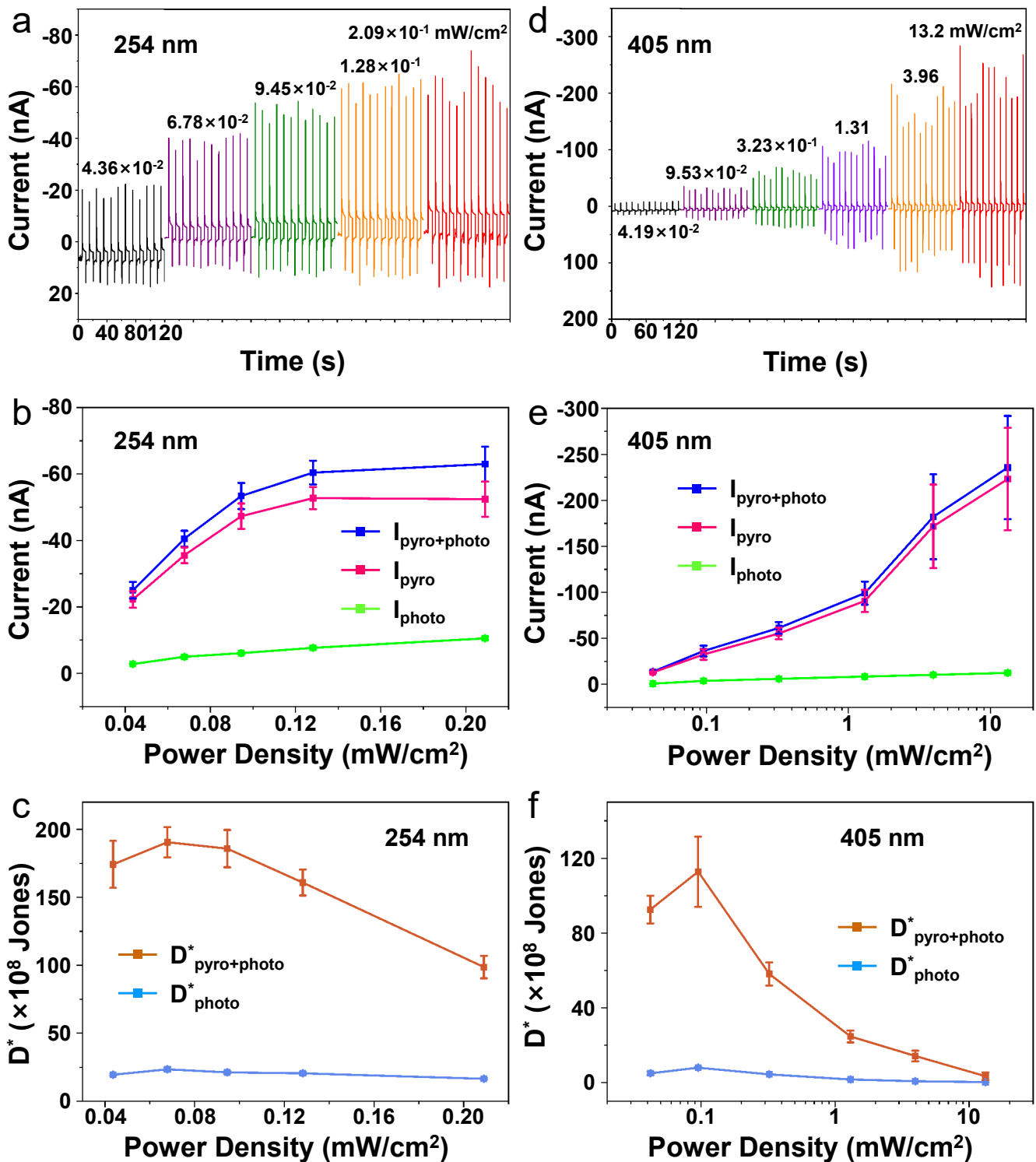
Figure 3. Pyro-phototronic effect in MXene/ZnO heterojunction nanogenerators. Transient current at 0 V bias under (**a**) 254 and (**d**) 405 nm illumination with different power densities. Three current components under (**b**) 254 and (**e**) 405 nm illumination. The specific detectivities under (**c**) 254 and (**f**) 405 nm illumination.

Furthermore, according to Figures 2 and 3, the detectivity of the MXene/ZnO heterojunction to all three wavelength illuminations tends to first increase and then gradually decrease. The difference is that when illuminated by UV light (254 nm and 365 nm), the increase in detectivity at low power density is not very obvious. But when illuminated by

405 nm light, the detectivity's increase becomes more distinctive. This phenomenon might be caused by the nonlinear relation between the temperature variation rate dT/dt and the power density. Definitely, the dT/dt would increase with power density. However, at low power density, the increment of dT/dt should be larger than that at high power density since part of the incident light's power is wasted. A similar relationship could be observed between the photoresponse current and the power density. When the power density is small, nearly all the photo-excited carriers can be collected. Whereas a lot of photo-excited carriers would recombine and hence only partial photo-excited carriers could be collected at high power density. Consequently, the detectivity first increases a little and then gradually decreases. This could be solved by designing the device's surface morphology to optimize the light-induced heating ability.

Since the pyro-phototronic effect originates from the light-induced temperature variation rate dT/dt in ZnO, the as-fabricated MXene/ZnO heterojunction nanogenerator should be able to harvest other visible and even near-infrared illuminations. Figure 4a,b show the light wavelength (from deep UV to near-infrared) dependent transient current of MXene/ZnO heterojunction at 0 V bias. Obviously and consistently, the pyro-phototronic effect improves the current significantly under 254, 365, and 405 nm illuminations. However, for other light wavelengths, including 532, 648, 780, and 830 nm illuminations, both $I_{pyro+photo}$ and I_{photo} decrease greatly at a scale of only a few nanoamperes. As ZnO hardly absorbs visible and near-infrared illuminations, the temperature variation rate dT/dt should be very small. Consequently, the transient current originating from the light-induced temperature variation rate dT/dt also becomes very small. The responsivities for different light wavelengths have been calculated and plotted in Figure 4c. It shows the same modulations by the pyro-phototronic effect. Here, since the response currents under visible and near-infrared illuminations are too small (~a few nanoamperes), the corresponding responsivities are also much smaller than that under 254, 365, and 405 nm illuminations, at the scale of only a few μA/W. These results show the possible ability of the MXene/ZnO heterojunction nanogenerator to harvest visible and near-infrared illuminations, but the performance still needs significant improvement. One possible solution is the introduction of a narrow bandgap semiconductor, which could better absorb the incident light.

The performance improvement resulting from the pyro-phototronic effect has been further investigated under high-temperature conditions. Since the pyro-phototronic effect is induced by light-induced temperature variation rate dT/dt of ZnO, it is expected that performance improvement by the pyro-phototronic effect could be further strengthened by lowering the temperature. Therefore, it is hard to perform the pyro-phototronic effect under high-temperature conditions. Figure 4d presents the I–V characteristics of MXene/ZnO heterojunction under dark and different temperature conditions. When the temperature increases from room temperature (RT) to 200 °C, the reverse current remains almost unchanged, and the forward current increases to some degree. While the temperature further increases to 300 °C, both reverse and forward currents increase greatly, indicating the reduction in rectification behavior of MXene/ZnO heterojunction. Figure 4e–h show the transient current of MXene/ZnO heterojunction under 0.276 mW/cm^2 365 nm UV illumination with different temperatures. It is obvious that the pyro-phototronic effect works very well under RT and 120 °C. However, it vanishes under a high temperature of 300 °C. This is because of the high dark current I_{dark} (~hundreds of nanoamperes) and the weak heating ability of light illumination at a high temperature of 300 °C. Fascinatingly, though the pyro-phototronic effect is largely reduced, it could still work at 200 °C, presenting an $I_{pyro+photo}$ of ~a few dozen nanoamperes. These results clearly show the potential of a pyro-phototronic effect-enhanced light energy harvesting nanogenerator at high temperatures.
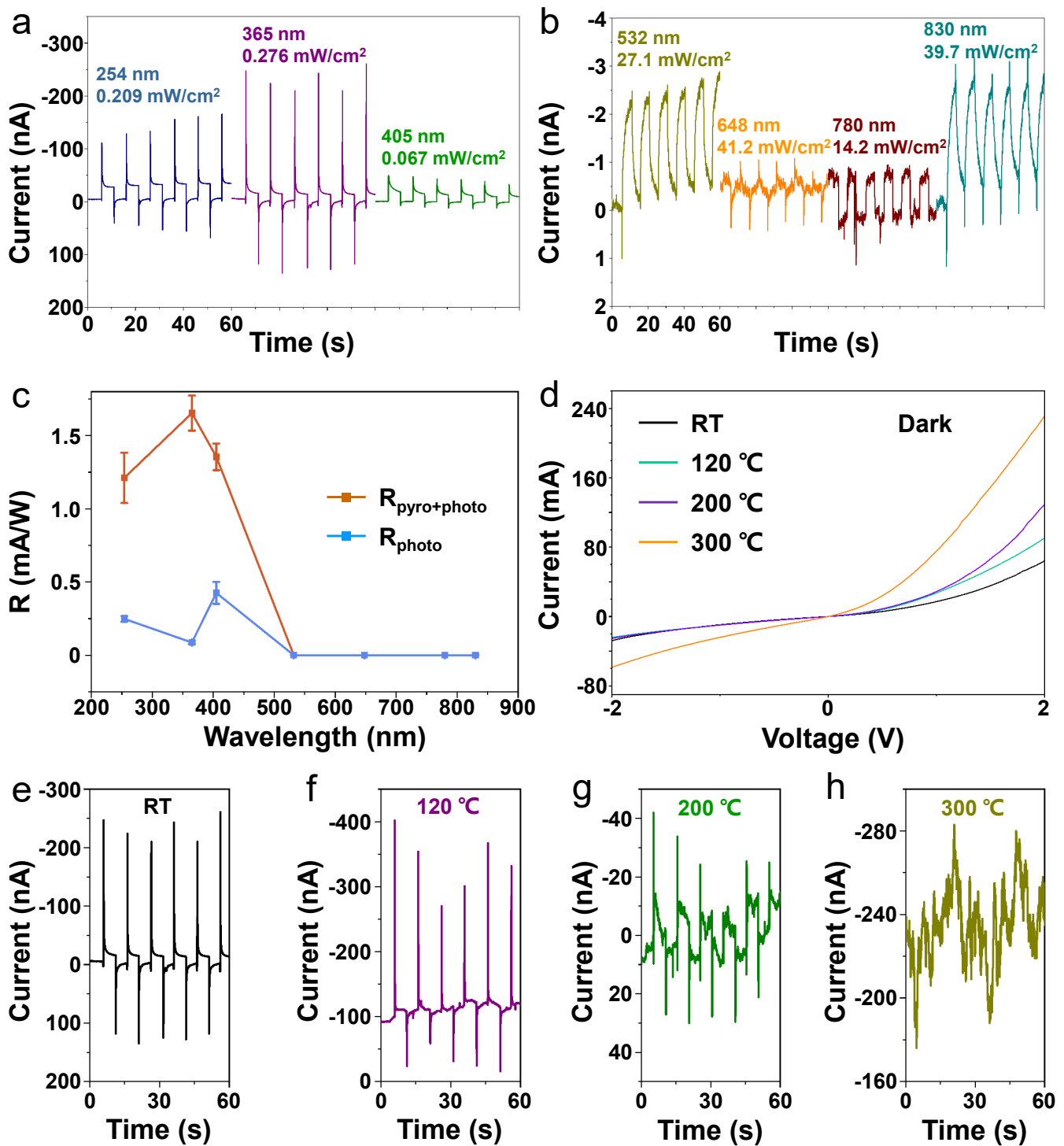
Figure 4. Broadband and high–temperature performances: (**a**,**b**) transient current at different light wavelengths, (**c**) responsivity at different light wavelengths, (**d**) I–V characteristics under dark conditions at different temperatures, and (**e**–**h**) transient current at different temperatures.

To investigate the influence of the ZnO layer on the pyro-phototronic effect in MXene/ZnO heterojunction nanogenerators, the hydrothermal method has been introduced to grow ZnO nanowires (NWs) on an ITO/glass substrate before spin-coating an MXene layer. The details of the hydrothermal growth of ZnO NWs can be found in the Section 2. Here, for simplification, MXene/ZnO NWs heterojunctions fabricated using different ZnO layers are numbered correspondingly, as indicated in Table 1. The #5 sample is the MXene/ZnO

heterojunction discussed above. So here, only the other four samples based on ZnO NWs are systematically investigated.

Table 1. Number of MXene/ZnO NWs heterojunctions fabricated using different ZnO layers.

Number	ZnO Thin Film or ZnO NWs	Growth Method	Figure
#1	ZnO NWs	25 mM $Zn(NO_3)_2$ + 12.5 mM HMTA + 5.4 mL NH_4OH, 95 °C, 1 h	Figure S6
#2	ZnO NWs	25 mM $Zn(NO_3)_2$ + 25 mM HMTA, 80 °C, 3 h	Figure S7
#3	ZnO NWs	50 mM $Zn(NO_3)_2$ + 50 mM HMTA, 80 °C, 3 h	Figure S8
#4	ZnO NWs	100 mM $Zn(NO_3)_2$ + 100 mM HMTA, 80 °C, 3 h	Figure S9
#5	ZnO thin film	Sputtering, RT, 30 min	Figures 1–3 and S5

The top and cross-sectional SEM images, I–V characteristics, and transient current at 0 V bias under 365 and 405 nm illuminations are summarized in Figures S6–S9, respectively. All the cross-sectional SEM images show the well-grown ZnO NWs on the ZnO seed layer but with different NW lengths and diameters. The ZnO NWs grown in higher concentration solutions show larger diameters. While the ZnO NWs grown with ammonia own larger length. All top SEM images indicate good coverage of ZnO NWs by spin-coated MXene layer, and the surfaces of MXene layers are all smooth and uniformly distributed. The I–V characteristics validate the good contact between the MXene layer and ZnO NWs, presenting good rectification behavior and excellent response to 365 and 405 nm illuminations. However, compared to the MXene/ZnO heterojunction based on ZnO thin film, the four samples based on ZnO NWs have much weaker pyro-phototronic effect modulation. These results are attributable to the long ZnO NWs. When the incident light illuminates on the MXene/ZnO heterojunction, photons would be absorbed mainly in the top region of ZnO. As a consequence, electrons and holes are mainly produced in the top region, and the temperature variation also happens mainly in the top region. For the MXene/ZnO heterojunction based on ZnO thin film, because the thickness of ZnO thin film is relatively small, on the one hand, the photo-generated carriers could transport to the MXene layer and bottom ITO layer for collection; on the other hand, the temperature variation rate of whole ZnO thin film is apparent. These two conditions together yield excellent pyro-phototronic effect modulation in MXene/ZnO heterojunction based on ZnO thin film. However, for MXene/ZnO heterojunction based on ZnO NWs, because the length of ZnO NWs is relatively large, the photo-generated carriers could hardly transport to electrodes for collection. Meanwhile, since only the top region of ZnO NWs is heated by illumination, the temperature variation rate of the whole ZnO NWs should be relatively small. Consequently, the pyro-phototronic effect modulation is much weaker in MXene/ZnO heterojunction based on ZnO NWs. If the pyro-phototronic effect is not considered, i.e., a forward +2 V bias is applied instead of 0 V bias, the responses of MXene/ZnO heterojunctions based on ZnO NWs would outperform the one based on ZnO thin film. As clearly shown in Figure S10, both R and D* at forward +2 V bias under 365 and 405 nm illuminations of the four ZnO NWs-based samples are larger than that of the #5 sample.

Furthermore, the influence of the rotation speed during the spin-coating of the MXene layer on the pyro-phototronic effect in the MXene/ZnO heterojunction nanogenerator has been systematically studied. The rotation speed is controlled at 1000 rpm for the MXene/ZnO heterojunction discussed above. Here, it is controlled at three other speeds, including 800, 500, and 0 rpm. The 0 rpm means that the MXene solution is directly dropped onto the surface of the ZnO layer without rotation. ZnO thin film synthesized by sputtering for 30 min is chosen for all the heterojunctions studied here. The SEM

images and corresponding I–V characteristics are plotted in Figure S11a1–a3 and S11b1–b3, respectively. As shown in Figure S11a1–a3, with the decrease in rotation speed, the thickness of the MXene layer gradually increases, with ~500 nm at 0 rpm. Compared to the I–V characteristic shown in Figure 1d, the ones shown in Figure S11b1–b3 present weaker rectification behavior and poor response to 365 nm UV illumination at forward +2 V bias. However, these three MXene/ZnO heterojunctions based on different rotation speeds during the spin-coating of the MXene layer exhibit a good pyro-phototronic effect, as illustrated in Figure 5a,c,e. From Figure 5a,c, when the rotation speed decreases from 1000 rpm to 800/500 rpm, the pyroelectric current spike I_{pyro} has been greatly enhanced from ~−100 nA (on average) to ~−250 nA/~−150 nA (on average). While the rotation speed further decreases to 0 rpm, I_{pyro} decreases to ~−40 nA (on average), as shown in Figure 5e. These results are due to the trade-off between carrier transportation and the temperature variation rate of ZnO. When the thickness of MXene is increased from ~35 nm (Figure 1c) to hundreds of nanometers, the formation of the MXene layer is more solid and compact, therefore enhancing carrier transportation. However, the increase in the MXene layer's thickness would of course affect the temperature variation rate of ZnO to some degree, which reduces the pyroelectric effect in ZnO. Due to the combination of these two conditions, the pyro-phototronic effect is enhanced first and then decreased with decreasing rotation speed.
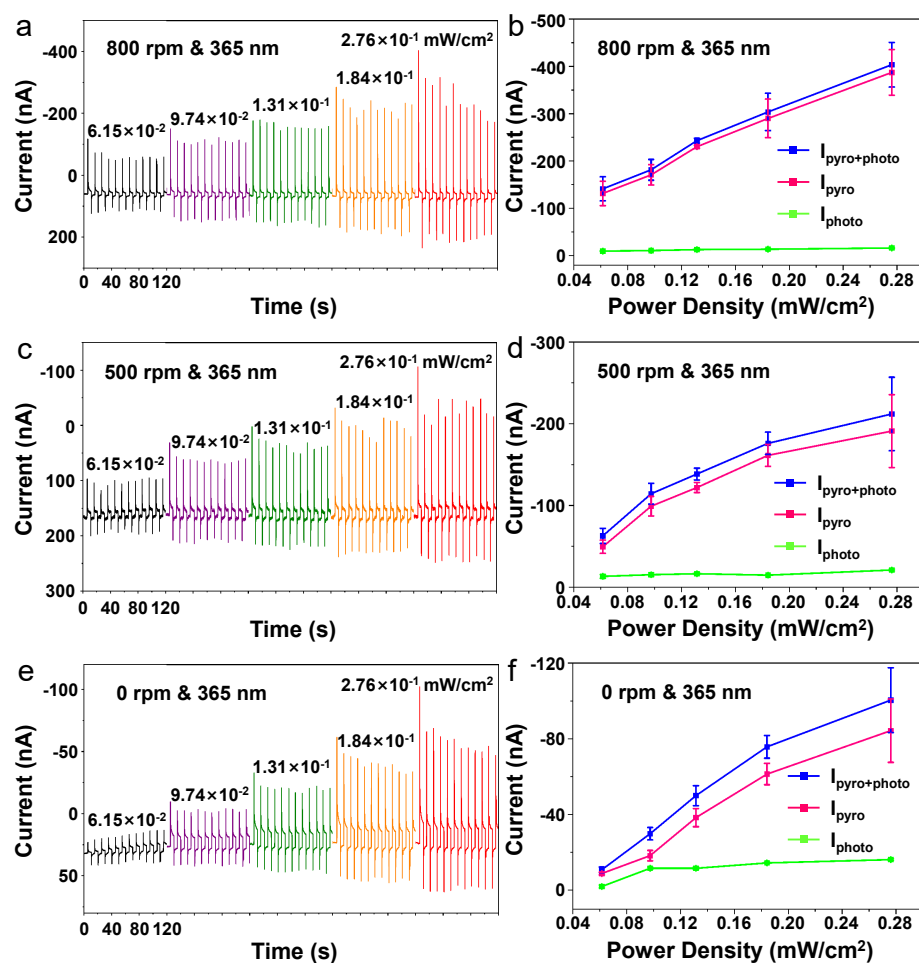
Figure 5. Influence of rotation speed during the spin–coating of the MXene layer. The transient current of MXene/ZnO heterojunctions with rotation speeds of (**a**) 800 rpm, (**c**) 500 rpm, and (**e**) 0 rpm. Three current components of MXene/ZnO heterojunctions with rotation speeds of (**b**) 800 rpm, (**d**) 500 rpm, and (**f**) 0 rpm.

The three current components of these three heterojunctions are derived and summarized in Figure 5b,d,f, clearly indicating the excellent pyro-phototronic effect-induced enhancement, regardless of the influence of the MXene layer's thickness. Then, the responsivity, its relative variation, and specific detectivity have been calculated and summarized in Figure S11c–e, respectively. The corresponding results of the heterojunction with 1000 rpm rotation speed have also been added for comparison. The results clearly show that the optimized rotation speed during the spin-coating of the MXene layer is 800 rpm, possessing the largest responsivity and its relative variation, and also similar specific detectivity compared to the case of 1000 rpm. In the case of 500 rpm, the responsivity and its relative variation are comparable to the case of 1000 rpm, whereas the specific detectivity is much smaller.

Because ZnO is a semiconductor material owning both pyroelectricity and piezoelectricity, it is reasonable to couple the pyro-phototronic effect with the piezo-phototronic effect in ZnO. The MXene/ZnO heterojunction nanogenerator has been further fabricated on a flexible ITO/PET substrate with the same fabrication processes. The details can be found in the Section 2. The responses of this flexible MXene/ZnO heterojunction nanogenerator to 254, 365, and 405 nm illuminations are derived, calculated, and summarized in Figures S12 and S13. The pyro-phototronic effect greatly enhances the performances in all three light wavelengths, demonstrating excellent device characteristics on a flexible substrate. Furthermore, by integrating a 3D stage into the measurement system, compressive and tensile strains can be feasibly applied to the flexible MXene/ZnO heterojunction nanogenerator, as shown in Figure 6a. The calculation of applied strain can be found in Figure S14 and Supporting Information. Under 59.6 $\mu W/cm^2$ 405 nm visible illumination, different strains are applied to the flexible MXene/ZnO heterojunction nanogenerator to investigate the coupling between pyro-phototronic and piezo-phototronic effects. As clearly shown in Figure 6b, with an increase in compressive strain, the pyroelectric current spike I_{pyro} gradually decreases; with an increase in tensile strain, the pyroelectric current spike I_{pyro} first increases a little and then gradually decreases. Different to the pyroelectric current spike I_{pyro}, photovoltaic effect-induced current I_{photo} remains nearly unchanged under different compressive and tensile strains. Figures 6c,d and S15 present the three current components, responsivity, and specific detectivity as functions of applied strain, showing that the coupling of piezo-phototronic and pyro-phototronic effects is valid and can modulate the performance of the MXene/ZnO heterojunction nanogenerator, with reductions observed at most strains. Only by applying a very small tensile strain can the performances be improved.

The working mechanism of the cooperation between pyro-phototronic and piezo-phototronic effects is carefully analyzed and schematically illustrated in Figure 7. Figure 7a is the energy band diagram of MXene/ZnO heterojunction under dark conditions, showing a Schottky junction-type rectification energy band diagram. While a small tensile strain is applied, a small amount of positive piezoelectric charges is produced at the MXene/ZnO heterojunction interface, only slightly lowering the Schottky barrier height. Since the Schottky barrier height is only slightly lowered due to positive piezoelectric charges, the depletion region, as well as the electric field, is also narrowed/weakened slightly, which has negligible influence on the response to light illumination. Meanwhile, positive pyroelectric charges are produced at the MXene/ZnO heterojunction interface upon the illumination, owning the same polarity of piezoelectric charges and thus enhancing the pyroelectric current spike I_{pyro}, as illustrated in Figure 7b. When the tensile strain further increases, more positive piezoelectric charges are produced at the MXene/ZnO heterojunction interface, reducing the Schottky barrier height significantly and even converting the Schottky junction-type energy band diagram into Ohmic contact type. Under such a circumstance, the electron depletion region becomes an electron accumulation region, and the direction of the electric field reverses. Though the MXene/ZnO heterojunction still could respond to incident light illumination, the Schottky barrier disappears. As a result, free electrons would accumulate near the interface, weakening the effective positive piezoelectric and pyroelectric charges and reducing I_{pyro}, as illustrated in Figure 7c. In

the case of compressive strain, as illustrated in Figure 7d, negative piezoelectric charges are produced at the MXene/ZnO heterojunction interface, increasing the Schottky barrier height. This should be good for the generation and separation of photo-generated electrons and holes. However, the polarities of piezoelectric charges and pyroelectric charges are contrary, the former being negative and the latter being positive, resulting in the continuous reduction in I_{pyro}. These experimental results and corresponding working mechanisms all prove the effective coupling between pyro-phototronic and piezo-phototronic effects in the MXene/ZnO heterojunction nanogenerator. Further optimization towards their coupling phenomenon is required to possess improvement in the performances instead of reduction.
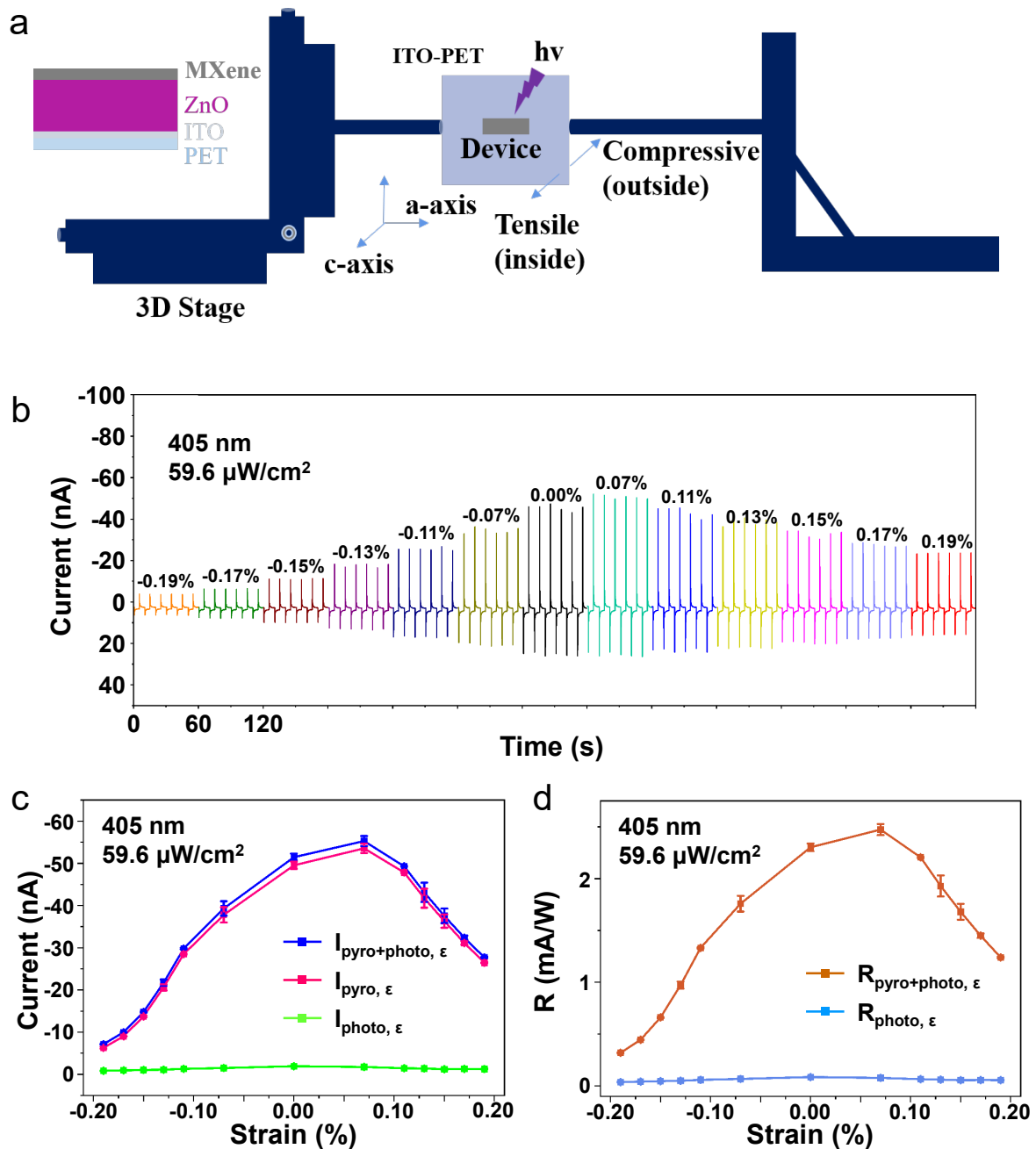
Figure 6. Coupling of pyro-phototronic and piezo-phototronic effects: (**a**) device structure of flexible MXene/ZnO heterojunction nanogenerator and the system to apply strain, (**b**) transient current under different strains, (**c**) the three current components, and (**d**) responsivity under different strains.
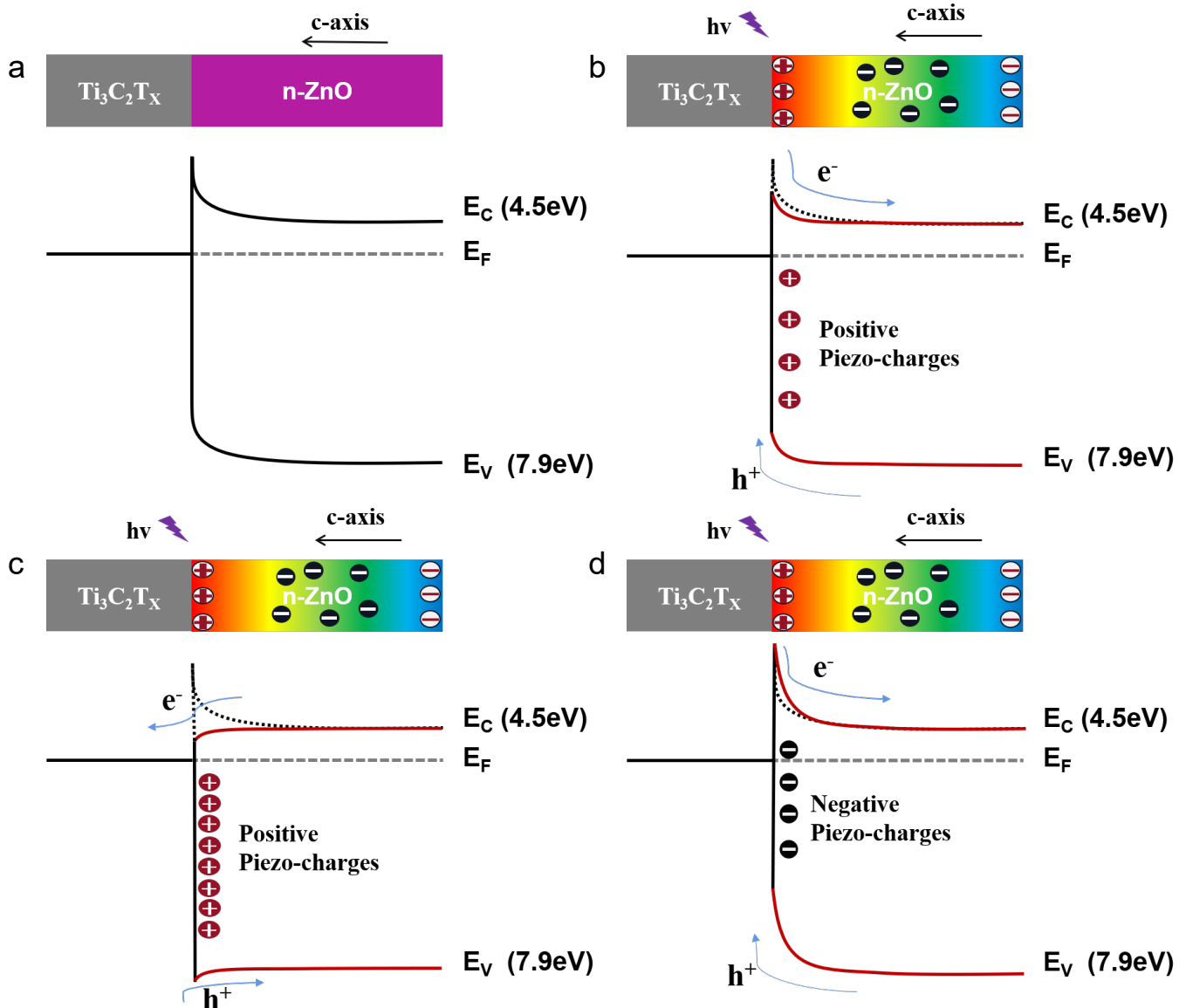
Figure 7. The working mechanism of coupling between the pyro-phototronic effect and piezo-phototronic effect. Energy band diagram of MXene/ZnO heterojunction nanogenerator under (**a**) dark conditions, (**b**) small tensile strain, (**c**) large tensile strain, and (**d**) compressive strain.

4. Conclusions

In this work, an MXene/ZnO heterojunction is demonstrated as a light energy harvesting nanogenerator, and the pyro-phototronic effect has been successfully introduced to enhance the nanogenerator's performances. For the MXene/ZnO thin-film heterojunction nanogenerator under 365 nm UV illumination, the current can be enhanced from only a few nanoamperes to ~ -140 nA, the responsivity from ~ 0.1 mA/W to ~ 1.3 mA/W, and the specific detectivity from 20×10^8 to 160×10^8 Jones. Moreover, the pyro-phototronic can still work at a high temperature of 200 °C. Additionally, the influences of ZnO and MXene layers have been carefully studied. The results indicate that the thicknesses of the ZnO layer and MXene layer should be carefully chosen to optimize the pyro-phototronic effect-induced modulation in performances. Longer ZnO NWs lead to better performance at forward bias but weaker pyro-phototronic effect. While the MXene layer has an optimum thickness to simultaneously enhance the carrier transportation and temperature variation rate in ZnO. Then, the coupling of pyro-phototronic and piezo-phototronic effects has been validated in MXene/ZnO heterojunction nanogenerators, implying that only a small

tensile strain could improve performance. These results show the huge potential of the pyro-phototronic effect in heterojunction-based light energy harvesting nanogenerators.

Though the reported spin-coated MXene layer could simultaneously form good Schottky contact with ZnO and enhance the thermal conductivity to have a better light-induced pyro-phototronic effect, the output current is still at the level of hundreds of nA, and the responsivity is only a few mA/W, which significantly hinder the practical applications of pyro-phototronic nanogenerators. Efforts should be made from developing novel pyro-electric semiconductor materials to optimizing device structure and surface morphology for further improvement of the output current and responsivity of the pyro-phototronic nanogenerator. Moreover, pyro-phototronic nanogenerators generally cannot work in high-temperature environments, since pyroelectricity is highly sensitive to temperature. Therefore, it is also necessary to develop high-temperature pyro-phototronic nanogenerators for applications in extreme environments.

Author Contributions: M.X.: Data curation; Formal analysis; Investigation; Validation; Visualization; Writing—original draft; Writing—review & editing. F.L.: Conceptualization; Data curation; Formal analysis; Methodology; Validation; Visualization; Writing—original draft; Writing—review & editing. W.P.: Conceptualization; Data curation; Methodology; Project administration; Supervision; Validation; Writing—original draft; Writing—review & editing. Q.Z.: Funding acquisition; Resources; Writing—review & editing. Y.H.: Conceptualization; Funding acquisition; Supervision; Writing—review & editing. All authors have read and agreed to the published version of the manuscript.

References

1. Wang, X.; Song, J.; Liu, J.; Wang, Z.L. Direct-Current Nanogenerator Driven by Ultrasonic Waves. *Science* **2007**, *316*, 102–105. [CrossRef] [PubMed]
2. Fan, F.R.; Tang, W.; Wang, Z.L. Flexible Nanogenerators for Energy Harvesting and Self-Powered Electronics. *Adv. Mater.* **2016**, *28*, 4283–4305. [CrossRef] [PubMed]
3. Wu, C.; Wang, A.C.; Ding, W.; Guo, H.; Wang, Z.L. Triboelectric Nanogenerator: A Foundation of the Energy for the New Era. *Adv. Energy Mater.* **2018**, *9*, 1802906. [CrossRef]
4. Wang, Z.L. Triboelectric Nanogenerator (TENG)—Sparking an Energy and Sensor Revolution. *Adv. Energy Mater.* **2020**, *10*, 2000137. [CrossRef]
5. Wang, Z.L.; Song, J. Piezoelectric Nanogenerators Based on Zinc Oxide Nanowire Arrays. *Science* **2006**, *312*, 242–246. [CrossRef]
6. Fan, F.-R.; Tian, Z.-Q.; Wang, Z.L. Flexible triboelectric generator. *Nano Energy* **2012**, *1*, 328–334. [CrossRef]
7. Wang, Z.L. On Maxwell's displacement current for energy and sensors: The origin of nanogenerators. *Mater. Today* **2017**, *20*, 74–82. [CrossRef]
8. Wang, Z.L. On the first principle theory of nanogenerators from Maxwell's equations. *Nano Energy* **2020**, *68*, 104272. [CrossRef]
9. Wang, Z.L. On the expanded Maxwell's equations for moving charged media system—General theory, mathematical solutions and applications in TENG. *Mater. Today* **2022**, *52*, 348–363. [CrossRef]
10. Wang, Z.L. From contact electrification to triboelectric nanogenerators. *Rep. Prog. Phys.* **2021**, *84*, 096502. [CrossRef]
11. Yang, W.; Chen, J.; Jing, Q.; Yang, J.; Wen, X.; Su, Y.; Zhu, G.; Bai, P.; Wang, Z.L. 3D Stack Integrated Triboelectric Nanogenerator for Harvesting Vibration Energy. *Adv. Funct. Mater.* **2014**, *24*, 4090–4096. [CrossRef]
12. Park, J.Y.; Salauddin; Rasel, M.S. Nanogenerator for scavenging low frequency vibrations. *J. Micromech. Microeng.* **2019**, *29*, 053001. [CrossRef]
13. Chen, J.; Wang, Z.L. Reviving Vibration Energy Harvesting and Self-Powered Sensing by a Triboelectric Nanogenerator. *Joule* **2017**, *1*, 480–521. [CrossRef]
14. Yang, J.; Chen, J.; Yang, Y.; Zhang, H.; Yang, W.; Bai, P.; Su, Y.; Wang, Z.L. Broadband Vibrational Energy Harvesting Based on a Triboelectric Nanogenerator. *Adv. Energy Mater.* **2013**, *4*, 1301322. [CrossRef]
15. Zhang, H.; Yang, Y.; Su, Y.; Chen, J.; Adams, K.; Lee, S.; Hu, C.; Wang, Z.L. Triboelectric Nanogenerator for Harvesting Vibration Energy in Full Space and as Self-Powered Acceleration Sensor. *Adv. Funct. Mater.* **2014**, *24*, 1401–1407. [CrossRef]
16. Cui, N.; Gu, L.; Liu, J.; Bai, S.; Qiu, J.; Fu, J.; Kou, X.; Liu, H.; Qin, Y.; Wang, Z.L. High performance sound driven triboelectric nanogenerator for harvesting noise energy. *Nano Energy* **2015**, *15*, 321–328. [CrossRef]
17. Fan, X.; Chen, J.; Yang, J.; Bai, P.; Li, Z.; Wang, Z.L. Ultrathin, Rollable, Paper-Based Triboelectric Nanogenerator for Acoustic Energy Harvesting and Self-Powered Sound Recording. *ACS Nano* **2015**, *9*, 4236–4243. [CrossRef]
18. Rani, G.M.; Wu, C.-M.; Motora, K.G.; Umapathi, R.; Jose, C.R.M. Acoustic-electric conversion and triboelectric properties of nature-driven CF-CNT based triboelectric nanogenerator for mechanical and sound energy harvesting. *Nano Energy* **2023**, *108*, 108211. [CrossRef]
19. Hou, T.-C.; Yang, Y.; Zhang, H.; Chen, J.; Chen, L.-J.; Wang, Z.L. Triboelectric nanogenerator built inside shoe insole for harvesting walking energy. *Nano Energy* **2013**, *2*, 856–862. [CrossRef]
20. Wang, J.; Li, S.; Yi, F.; Zi, Y.; Lin, J.; Wang, X.; Xu, Y.; Wang, Z.L. Sustainably powering wearable electronics solely by biomechanical energy. *Nat. Commun.* **2016**, *7*, 12744. [CrossRef]
21. Xie, Y.; Wang, S.; Lin, L.; Jing, Q.; Lin, Z.-H.; Niu, S.; Wu, Z.; Wang, Z.L. Rotary Triboelectric Nanogenerator Based on a Hybridized Mechanism for Harvesting Wind Energy. *ACS Nano* **2013**, *7*, 7119–7125. [CrossRef] [PubMed]
22. Wang, Z.L.; Jiang, T.; Xu, L. Toward the blue energy dream by triboelectric nanogenerator networks. *Nano Energy* **2017**, *39*, 9–23. [CrossRef]
23. Jiang, T.; Pang, H.; An, J.; Lu, P.; Feng, Y.; Liang, X.; Zhong, W.; Wang, Z.L. Robust Swing-Structured Triboelectric Nanogenerator for Efficient Blue Energy Harvesting. *Adv. Energy Mater.* **2020**, *10*, 2000064. [CrossRef]
24. Liu, G.; Guo, H.; Xu, S.; Hu, C.; Wang, Z.L. Oblate spheroidal triboelectric nanogenerator for all-weather blue energy harvesting. *Adv. Energy Mater.* **2019**, *9*, 1900801. [CrossRef]
25. Wen, Z.; Guo, H.; Zi, Y.; Yeh, M.-H.; Wang, X.; Deng, J.; Wang, J.; Li, S.; Hu, C.; Zhu, L.; et al. Harvesting Broad Frequency Band Blue Energy by a Triboelectric–Electromagnetic Hybrid Nanogenerator. *ACS Nano* **2016**, *10*, 6526–6534. [CrossRef]
26. Yang, Y.; Guo, W.; Pradel, K.C.; Zhu, G.; Zhou, Y.; Zhang, Y.; Hu, Y.; Lin, L.; Wang, Z.L. Pyroelectric Nanogenerators for Harvesting Thermoelectric Energy. *Nano Lett.* **2012**, *12*, 2833–2838. [CrossRef]

27. Yang, Y.; Wang, S.; Zhang, Y.; Wang, Z.L. Pyroelectric Nanogenerators for Driving Wireless Sensors. *Nano Lett.* **2012**, *12*, 6408–6413. [CrossRef]

28. Yang, Y.; Zhou, Y.; Wu, J.M.; Wang, Z.L. Single Micro/Nanowire Pyroelectric Nanogenerators as Self-Powered Temperature Sensors. *ACS Nano* **2012**, *6*, 8456–8461. [CrossRef]

29. Yang, Y.; Jung, J.H.; Kil Yun, B.; Zhang, F.; Pradel, K.C.; Guo, W.; Wang, Z.L. Flexible Pyroelectric Nanogenerators using a Composite Structure of Lead-Free $KNbO_3$ Nanowires. *Adv. Mater.* **2012**, *24*, 5357–5362. [CrossRef]

30. Zhang, K.; Wang, Y.; Wang, Z.L.; Yang, Y. Standard and figure-of-merit for quantifying the performance of pyroelectric nanogenerators. *Nano Energy* **2018**, *55*, 534–540. [CrossRef]

31. Wang, Z.; Yu, R.; Pan, C.; Li, Z.; Yang, J.; Yi, F.; Wang, Z.L. Light-induced pyroelectric effect as an effective approach for ultrafast ultraviolet nanosensing. *Nat. Commun.* **2015**, *6*, 8401. [CrossRef] [PubMed]

32. Wang, Z.; Yu, R.; Wang, X.; Wu, W.; Wang, Z.L. Ultrafast Response p-Si/n-ZnO Heterojunction Ultraviolet Detector Based on Pyro-Phototronic Effect. *Adv. Mater.* **2016**, *28*, 6880–6886. [CrossRef] [PubMed]

33. Sahare, S.; Ghoderao, P.; Sharma, M.K.; Solovan, M.; Aepuru, R.; Kumar, M.; Chan, Y.; Ziółek, M.; Lee, S.L.; Lin, Z.H. Pyro-phototronic effect: An effective route toward self-powered photodetection. *Nano Energy* **2023**, *107*, 108172. [CrossRef]

34. Dong, J.; Wang, Z.; Wang, X.; Wang, Z.L. Temperature dependence of the pyro-phototronic effect in self-powered p-Si/n-ZnO nanowires heterojuncted ultraviolet sensors. *Nano Today* **2019**, *29*, 100798. [CrossRef]

35. Zhang, Y.; Wang, Y.-C.; Wang, L.; Zhu, L.; Wang, Z.L. Highly Sensitive Photoelectric Detection and Imaging Enhanced by the Pyro-Phototronic Effect Based on a Photoinduced Dynamic Schottky Effect in 4H-SiC. *Adv. Mater.* **2022**, *34*, 2204363. [CrossRef] [PubMed]

36. Ouyang, B.; He, W.; Wu, L.; Zhao, L.D.; Yang, Y. Thermo-phototronic effect in p-type Na-doped SnS single crystals for enhanced self-powered photodetectors. *Nano Energy* **2021**, *88*, 106268. [CrossRef]

37. Silva, J.P.B.; Vieira, E.M.F.; Gwozdz, K.; Kaim, A.; Goncalves, L.M.; MacManus–Driscoll, J.L.; Hoye, R.L.Z.; Pereira, M. High-performance self-powered photodetectors achieved through the pyro-phototronic effect in $Si/SnO_x/ZnO$ heterojunctions. *Nano Energy* **2021**, *89*, 106347. [CrossRef]

38. Wang, L.; Xue, H.; Zhu, M.; Gao, Y.; Wang, Z. Graded strain-enhanced pyro-phototronic photodetector with a broad and plateau band. *Nano Energy* **2022**, *97*, 107163. [CrossRef]

39. Kumar, M.; Patel, M.; Kim, J.; Lim, D. Enhanced broadband photoresponse of a self-powered photodetector based on vertically grown SnS layers via the pyro-phototronic effect. *Nanoscale* **2017**, *9*, 19201–19208. [CrossRef]

40. Ma, J.; Chen, M.; Qiao, S.; Guo, S.; Chang, J.; Fu, G.; Wang, S. A new approach for broadband photosensing based on Ag2Se/Si heterojunction tuned by Pyro-phototronic effect. *Nano Energy* **2023**, *107*, 108167. [CrossRef]

41. Li, F.; Peng, W.; Pan, Z.; He, Y. Rationally designed piezoelectric charge polarity at interfaces for largely improving photodiode performance by piezo-phototronic effects. *J. Mater. Chem. C* **2020**, *8*, 16057–16066. [CrossRef]

42. Li, F.; Peng, W.; Pan, Z.; He, Y. Optimization of Si/ZnO/PEDOT:PSS tri-layer heterojunction photodetector by piezo-phototronic effect using both positive and negative piezoelectric charges. *Nano Energy* **2018**, *48*, 27–34. [CrossRef]

43. Xue, M.; Peng, W.; Tang, X.; Cai, Y.; Li, F.; He, Y. Pyro-Phototronic Effect Enhanced Pyramid Structured p-Si/n-ZnO Nanowires Heterojunction Photodetector. *ACS Appl. Mater. Interfaces* **2023**, *15*, 4677–4689. [CrossRef] [PubMed]

44. Peng, W.; Wang, C.; Li, F.; He, Y. Piezo- and photo-voltage field-effect transistor. *Nano Energy* **2023**, *105*, 108025. [CrossRef]

45. Li, F.; Peng, W.; He, Y. Bilateral piezoelectric charge modulation as a perspective of piezo-phototronic effect in tri-/multi-layer structured optoelectronics. *Nano Energy* **2023**, *113*, 108537. [CrossRef]

46. Dai, Y.; Wang, X.; Peng, W.; Zou, H.; Yu, R.; Ding, Y.; Wu, C.; Wang, Z.L. Largely Improved Near-Infrared Silicon-Photosensing by the Piezo-Phototronic Effect. *ACS Nano* **2017**, *11*, 7118–7125. [CrossRef]

47. Wang, X.; Yu, R.; Peng, W.; Wu, W.; Li, S.; Wang, Z.L. Temperature Dependence of the Piezotronic and Piezophototronic Effects in *a*-axis GaN Nanobelts. *Adv. Mater.* **2015**, *27*, 8067–8074. [CrossRef]

48. Pan, Z.; Peng, W.; Li, F.; Cai, Y.; He, Y. On the Piezo-Phototronic Effect in Si/ZnO Heterojunction Photodiode: The Effect of the Fermi-Level Difference. *Adv. Funct. Mater.* **2020**, *30*, 2005996. [CrossRef]

49. Tan, D.; Jiang, C.; Sun, N.; Huang, J.; Zhang, Z.; Zhang, Q.; Bu, J.; Bi, S.; Guo, Q.; Song, J. Piezoelectricity in monolayer MXene for nanogenerators and piezotronics. *Nano Energy* **2021**, *90*, 106528. [CrossRef]

50. Feng, Y.; He, M.; Liu, X.; Wang, W.; Yu, A.; Wan, L.; Zhai, J. Alternate-Layered MXene Composite Film-Based Triboelectric Nanogenerator with Enhanced Electrical Performance. *Nanoscale Res. Lett.* **2021**, *16*, 81. [CrossRef]

51. Tian, Y.; An, Y.; Xu, B. MXene-based materials for advanced nanogenerators. *Nano Energy* **2022**, *101*, 107556. [CrossRef]

52. Liu, R.; Li, W. High-Thermal-Stability and High-Thermal-Conductivity $Ti_3C_2T_x$ MXene/Poly(vinyl alcohol) (PVA) Composites. *ACS Omega* **2018**, *3*, 2609–2617. [CrossRef] [PubMed]

53. Jin, X.; Wang, J.; Dai, L.; Liu, X.; Li, L.; Yang, Y.; Cao, Y.; Wang, W.; Wu, H.; Guo, S. Flame-retardant poly(vinyl alcohol)/MXene multilayered films with outstanding electromagnetic interference shielding and thermal conductive performances. *Chem. Eng. J.* **2020**, *380*, 122475. [CrossRef]

54. Luo, Y.; Xie, Y.; Jiang, H.; Chen, Y.; Zhang, L.; Sheng, X.; Xie, D.; Wu, H.; Mei, Y. Flame-retardant and form-stable phase change composites based on MXene with high thermostability and thermal conductivity for thermal energy storage. *Chem. Eng. J.* **2021**, *420*, 130466. [CrossRef]

55. Pasupuleti, K.S.; Thomas, A.M.; Vidyasagar, D.; Rao, V.N.; Yoon, S.-G.; Kim, Y.-H.; Kim, S.-G.; Kim, M.-D. ZnO@Ti$_3$C$_2$T$_x$ MXene Hybrid Composite-Based Schottky-Barrier-Coated SAW Sensor for Effective Detection of Sub-ppb-Level NH$_3$ at Room Temperature under UV Illumination. *ACS Mater. Lett.* **2023**, *5*, 2739–2746. [CrossRef]

56. Rao, V.N.; Kwon, H.; Lee, Y.; Ravi, P.; Ahn, C.W.; Kim, K.; Yang, J.-M. Synergistic integration of MXene nanosheets with CdS@TiO$_2$ core@shell S-scheme photocatalyst for augmented hydrogen generation. *Chem. Eng. J.* **2023**, *471*, 144490.

57. Li, D.; Liu, G.; Zhang, Q.; Qu, M.; Fu, Y.Q.; Liu, Q.; Xie, J. Virtual sensor array based on MXene for selective detections of VOCs. *Sensors Actuators B Chem.* **2021**, *331*, 129414. [CrossRef]

58. Lu, Y.; Li, D.; Liu, F. Characterizing the Chemical Structure of Ti$_3$C$_2$T$_x$ MXene by Angle-Resolved XPS Combined with Argon Ion Etching. *Materials* **2022**, *15*, 307. [CrossRef]

59. Yergaliuly, G.; Soltabayev, B.; Kalybekkyzy, S.; Bakenov, Z.; Mentbayeva, A. Effect of thickness and reaction media on properties of ZnO thin films by SILAR. *Sci. Rep.* **2022**, *12*, 851. [CrossRef]

60. Khokhra, R.; Bharti, B.; Lee, H.-N.; Kumar, R. Visible and UV photo-detection in ZnO nanostructured thin films via simple tuning of solution method. *Sci. Rep.* **2017**, *7*, 15032. [CrossRef]